



Enhancing electrochemical nitrogen fixation by mimicking π back-donation on laser-tuned Lewis acid sites in noble-metal-molybdenum carbide

Bin Chang^{a,b,1}, Haifeng Yuan^{a,1}, Lili Li^c, Jiayuan Yu^a, Xiaoyu Liu^{a,d}, Wanqiang Yu^a, Bo Wang^{e,f}, Lili Zhao^a, Xiaoyan Liu^a, Shuhui Sun^b, Hong Liu^{a,d}, Weijia Zhou^{a,*}

^a Institute for Advanced Interdisciplinary Research (iAIR), School of Chemistry and Chemical Engineering, University of Jinan, Jinan 250022, PR China

^b Institut National de la Recherche Scientifique-Énergie Matériaux et Télécommunications, Varennes, Quebec J3X 1P7, Canada

^c Key Laboratory of Interfacial Physics and Technology, Shanghai Institute of Applied Physics, Chinese Academy of Sciences, Shanghai 201800, PR China

^d State Key Lab of Crystal Materials, Shandong University, Jinan 250100, PR China

^e State Key Laboratory of Photocatalysis on Energy and Environment, Fuzhou University, Fuzhou 350116, PR China

^f School of Materials Science and Engineering, University of Jinan, Jinan 250022, PR China

ARTICLE INFO

Keywords:

Laser synthesis
Lewis acid sites
 π back-donation
Molybdenum carbides
Electrochemical nitrogen fixation

ABSTRACT

Conventional electrocatalysts underperform with reaction kinetics, nitrogen dissociation, and activated hydrogen recombination, demanding effective strategies for improving electrochemical nitrogen fixation. The challenge lies in the rational design of electron back-donating centers for nitrogen activation and hydrogen migration path optimization. This study proposes an effective laser-tuning strategy to construct noble-metal Lewis acid sites on molybdenum carbide (M-Mo₂C, M = Ru, Rh, Pd, Ir), yielding a more active material system by mimicking π back-donation behavior. Laser-tuned Lewis acid sites can effectively break N \equiv N bonds, lower thermodynamic energy barrier of the rate-determining hydrogenation step ($^*NN \rightarrow ^*N-NH$), and optimize hydrogen migration pathway. The Rh-Mo₂C shows superior NRR activity with NH₃ yield of $\sim 26.3 \mu\text{g h}^{-1} \text{cm}_{\text{cat}}^{-2}$ and Faradaic efficiency of $\sim 15.4\%$, which are 5.1- and 3.6-fold higher than those of Mo₂C, respectively. This work demonstrates a unique and universal strategy for designing high-performance electrocatalysts by accurately manipulating electronic structure of active sites.

1. Introduction

Ammonia (NH₃) plays an important role in agriculture and industrial production [1]. The growing demand for NH₃ has stimulated the development of artificial nitrogen fixation, which is still limited by the N \equiv N activation barrier (bond energy 940.95 kJ mol⁻¹) [2–5]. Electrochemical nitrogen reduction reaction (NRR) is a promising alternative to the traditional Haber-Bosch process for producing NH₃ directly from abundant N₂ [6–10]. Electrochemical NRR is a three-step process: N₂ absorption, N₂ cleavage, and N-H formation by consecutive proton additions [11–13]. Unfortunately, NRR performance has been limited by the sluggish reaction kinetics of chemically inert N₂ and the competing hydrogen evolution reaction (HER) [14,15]. The preferential adsorption of hydrogen and unsuitable hydrogen migration path of the catalyst kinetically favors HER over NRR. Considering Lewis acid-base theory, Lewis pairs, well known for the ability to activate small molecules via

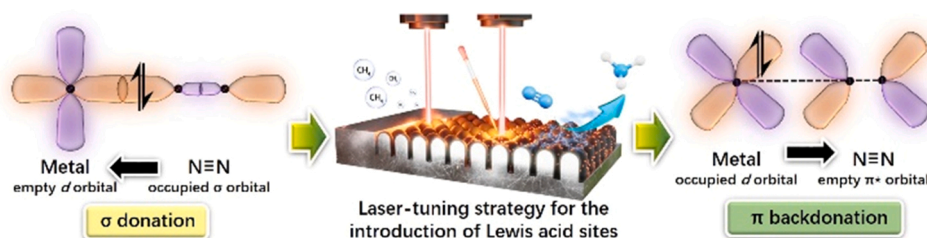
the concerted action of Lewis acid and Lewis base, have inspired an ever-widening scope of chemistry [16]. The rapid development of the catalysts with Lewis pairs sites has promoted research into heterogeneous catalysis with controllable materials synthesis, tunable micro-/nano/electronic structure, high surface area with abundant and accessible active sites and efficient mass transfer [17–19]. Herein, catalytic Lewis acid sites can easily adsorb Lewis bases, such as N₂ with lone pair electrons [20–23]. The rational design of optimized microstructures with effective active sites is the key focus to reduce the N \equiv N activation barrier and accelerate N-H formation.

The ideal NRR electrocatalyst has an excellent proton and N₂ activation ability accompanied by a suitable proton migration path to avoid HER [24]. Pioneering studies have extensively investigated routes toward surpassing the base NRR activity, including the use of noble-metal-based catalysts, transition metal compounds, and even metal-free catalysts [18,25–30]. Previously, boron Lewis acid catalytic

* Corresponding author.

E-mail address: ifc_zhouwj@ujn.edu.cn (W. Zhou).

¹ These authors contributed equally to this work



Scheme 1. Illustration of the design concept of laser tuned Lewis acid sites for mimicking π back-donation.

sites on carbon-based materials were constructed and showed that the empty sp^2 orbitals of these sites could promote the activation of N_2 with occupied p orbitals through π back-donation [18]. However, the electronic structure of boron with unoccupied orbitals lacks similarity to that of metals, which hinders further improvements in NRR activity. Furthermore, the incorporation of adsorbed H still limits further promotion. In transition-metal carbides, the metal sp hybridized states originate from the d states of the metal and s states of the carbon, which hybridize at the surface sites [31–34]. The excess of occupied orbitals at the metal sites results in electron back-donation to the π -antibonding orbitals of N_2 , endowing metal carbides with excellent N_2 cleavage ability [35–38]. Imparting Lewis acid character on adjacent transition-metal sites with empty orbitals via the introduction of noble metals has been proposed as a strategy for designing efficient NRR electrocatalysts. The precise construction of the active sites and optimization of the interfacial microstructures for enhanced nitrogen absorption remains the key objectives, though a suitable hydrogen migration path is also needed. Therefore, there is considerable interest in the modification of metal carbide materials with precisely modulated electronic structures for efficient NRR.

As a proof-of-concept, laser ablation synthesis was used due to its low energy consumption and energy localization [39–41] to introduce a series of noble-metal Lewis acid sites into molybdenum carbide ($M\text{-Mo}_2\text{C}$, $M = \text{Ru, Rh, Pd, Ir, Pt}$) (Scheme 1). The as-designed configuration can effectively achieve vital breakage of $N\equiv N$ bonds by mimicking π back-donation and lower the thermodynamic energy barrier of the hydrogenation steps and ammonia desorption step. Meanwhile, the introduction of noble-metal also optimized the migration path of active hydrogen, which further effectively inhibited the side reaction. This elegant and effective laser-tuning strategy not only enhances the NRR activity on Mo_2C but also guides the optimization of the interfacial microstructure and active sites for promoting π back-donation.

2. Experimental section

2.1. Chemicals

Ruthenium chloride, rhodium chloride, palladium chloride, hexachloroiridium acid hydrate, chloroplatinic acid hexahydrate, sodium sulfate were purchased from Macklin Biochemical Co., Ltd (Shanghai). $^{15}\text{N}_2$ was purchased from Maotou Gas Co., Ltd (Shanghai). In situ Raman electrolytic cell and matched Nafion 117 were purchased from Gaooss-Union Co., Ltd (Wuhan). The concentrated sulfuric acid (H_2SO_4) was purchased from the Far East Fine Chemical Co., Ltd (Yantai). High purity methane, nitrogen and argon gas were purchased from Deyang Gas Co., Ltd (Jinan). Molybdenum foils were purchased from Dahe New Energy Co., Ltd (Zhengzhou).

2.2. Materials synthesis

The purchased Mo foil was ultrasonically cleaned with dilute hydrochloric acid, alcohol, and deionized water in sequence before use. The molybdenum carbide pillars (Mo_2C) were laser scanned to convert

molybdenum substrates to Mo_2C at methane atmosphere. The basic laser parameters (LSF20D, Hgtech Laser, YLP-1–100–20–20-HC-RG) were 1064 nm (wavelength), 100 ns (pulse width), and 1 mJ (single pulse energy). A circular arrays mode was used in the laser ablation process. Meanwhile, the optimized laser parameters were the repetition rate of 20 kHz, the average power of 19 W, and the scanning speed of 500 mm s^{-1} .

The as-prepared Mo_2C precursor was laser processed to the size of $5 \times 5 \text{ mm}^2$. For the next step, the Mo_2C precursor was fully immersed in the 1 mL noble metal solutions of RuCl_3 , RhCl_3 , PdCl_2 , IrCl_3 and H_2PtCl_6 (2 mM), respectively. Subsequently, noble metal ion infiltrated Mo_2C precursor was scanned by laser at Ar/H_2 atmosphere. A linear scan mode was conducted in this laser reduction process. The optimized laser parameters were the average power of 7 W, the scanning speed of 500 mm s^{-1} , and the scanning spacing of 0.001 mm. Finally, the $\text{Ru}/\text{Rh}/\text{Pd}/\text{Ir}/\text{Pt}$ sites anchored molybdenum carbide pillars ($M\text{-Mo}_2\text{C}$, $M = \text{Ru, Rh, Pd, Ir, Pt}$) were successfully prepared.

2.3. Materials characterizations

Powder X-ray diffraction (XRD) patterns of the materials were obtained on a diffractometer (Rigaku Ultima IV, JPN) using a $\text{Cu K}\alpha$ radiation source ($\lambda = 0.15406 \text{ nm}$) with a 2θ scan from 10° to 90° with a step size of 0.04. X-ray photoelectron spectrometer (AXIS SUPRA, Kratos) with a monochromatic $\text{Al K}\alpha$ source and a charge neutralizer. All the binding energies were calibrated to the C 1s peak at 284.6 eV of the surface adventitious carbon. Scanning electron microscopy (SEM) images were collected using a Hitachi regulus 8100 microscope equipped with an energy-dispersive X-ray analyzer (EDS). Transmission electron microscopy (TEM) and high-resolution transmission electron microscopy (HRTEM) images were recorded on a JEOL JEM-2100Plus electron microscope at an accelerating voltage of 200 kV. The solution of samples was achieved after 20 min ultrasonic pretreatment. The TEM samples were prepared by dropping the primed solution onto a copper grid with polyvinyl formal support film and dried in air. ICP-MS results were achieved by Agilent ICP-OES 730.

The X-ray absorption spectra (XAS) including X-ray absorption near-edge structure (XANES) and extended X-ray absorption fine structure (EXAFS) were performed on beamline 1W1B station at the Beijing Synchrotron Radiation Facility (BSRF) and the Spring-8 14B2, where a pair of channel-cut Si (111) crystals was utilized in the monochromator. The storage ring was working at the energy of 8.0 GeV with average 99.5 mA electron current. The data reduction, data analysis, and EXAFS fitting were performed and analyzed with the Athena and Artemis programs of the Demeter data analysis packages [42] that use the FEFF6 program [43] to fit the EXAFS data. The energy calibration of the sample was conducted through a standard Rh foil, which as a reference was simultaneously measured. A linear function was subtracted from the pre-edge region, then the edge jump was normalized using Athena software. The $\chi(k)$ data were isolated by subtracting a smooth, two-stage polynomial approximating the absorption background of an isolated atom. The k^3 -weighted $\chi(k)$ data were Fourier transformed after applying a Hanning window function ($\Delta k = 1.0$). For EXAFS modeling, the global amplitude EXAFS (CN , R , σ^2 and ΔE_0) were obtained by

nonlinear fitting, with least-squares refinement, of the EXAFS equation to the Fourier-transformed data in R-space, using Artemis software, EXAFS of the Rh foil is fitted and the obtained amplitude reduction factor S_0^2 value (0.85) was set in the EXAFS analysis to determine the coordination numbers (CNs) in the scattering path in the sample. For Wavelet Transform analysis, the $\chi(k)$ exported from Athena was imported into the Hama Fortran code. The parameters were listed as follow: R range, 1–3.5 Å(Rh)/ 0.5–4.5 Å(Mo), k range, 0–12.5 Å⁻¹; k weight, 3; and Morlet function with $\kappa = 15$, $\sigma = 1$ was used as the mother wavelet to provide the overall distribution.

2.4. Electrochemical measurements

The electrocatalytic NRR tests were measured by using a two-compartment H-type like electrolytic cell, which was separated by a Nafion 117 membrane (DuPont). The Nafion membrane was pretreated by boiling it in H₂O₂ (5%) at 80 °C for 1 h and deionized water for another 1 h, sequentially. The electrochemical experiments were conducted with an electrochemical workstation (CHI 1000 C) by using a three-electrode configuration (working electrode of as-synthesized materials, counter electrode of Pt plate, and reference electrode of Ag/AgCl/saturated KCl). Before NRR tests, the cathode electrolyte was purged with high purity nitrogen (99.999%, 40 mL/min) for 0.5 h and then the flow rate was adjusted to 15 mL/min and maintained stable during the constant potential test for 3 h. The ammonia formation rate presented in the manuscript is the average data for the reaction of 3 h. In this work, all potentials were converted to the reversible hydrogen electrode (RHE) potential using the equation given by $E_{\text{RHE}} = E_{\text{Ag/AgCl}} + 0.0591 \times \text{pH} + 0.194$, resulting in a shift of +0.6077 V versus RHE (0.05 M Na₂SO₄, pH~7.1). Polarization curves were obtained using linear sweep voltammetry (LSV) with a scan rate of 2 mV·s⁻¹ at 25 °C in an aqueous solution (0.05 M Na₂SO₄) with constant N₂ (g) or Ar (g) continually purging for 30 min prior to the measurements. The polarization curves were the steady-state ones after several cycles. Electrochemical impedance spectroscopy (EIS) was carried out in the potentiostatic mode from 10⁵ to 0.01 Hz. The long-term stability test was carried out using chronoamperometry measurements.

2.5. Determination of ammonia

The concentration of produced ammonia was spectrophotometrically detected by the indophenol blue method same as previous reports [44,45]. In detail, a 2 mL aliquot of the solution was removed from the post-electrolysis electrolyte after the reaction. Then 2 mL NaOH solution (1 M) containing 5 wt% salicylic acid and 5 wt% sodium citrate was added, followed by 1 mL 0.05 M NaClO and 0.2 mL 1 wt% sodium nitroferricyanide (C₅FeN₆Na₂O) solution. After 1 h, the absorption spectra of the mixed solution were measured with an ultraviolet-visible spectrophotometer. The concentration of NH₃ was determined by absorbance at a wavelength of ~675 nm. Absolute calibration was achieved using NH₄⁺ of known concentration in 0.01 M HCl solutions as standards. The concentration of ammonia were determined by a standard curve (Absorbance = 0.08677 × C_{NH₃} - 0.04769, R² = 0.994).

The ammonia yield was calculated using the following equation:

$$\text{Yield}(\text{NH}_3) = \frac{c_{\text{NH}_3} \times V}{17 \times t \times A}$$

where c_{NH_3} is the measured ammonia concentration (μg mL⁻¹), V is the volume of the electrolyte solution (10 mL), t is the reaction time (3 h), A is the area of the working electrode (2 cm²). The Faradaic efficiency for NRR is defined as the quantity of electric charge used for synthesizing ammonia. The production of an NH₃ molecule theoretically needs three electrons. The Faradaic efficiency (FE) was calculated by the following equation:

$$\text{FE} = \frac{3F \times c_{\text{NH}_3} \times V}{17 \times I \times t} \times 100\%$$

Where F is Faraday constant (96485 C·mol⁻¹), c_{NH_3} is the measured ammonia concentration (μg mL⁻¹), V is the volume of the electrolyte solution (10 mL), I is the current (A), t is the reaction time (3 h).

The concentration of by-produced hydrazine (N₂H₄) was spectrophotometrically detected by using the method developed by Watt and Chrisp [46]. In detail, the color reagent was firstly prepared by mixing 2 mL hydrochloric acid, 0.4 g p-(dimethylamino) benzaldehyde and 20 mL ethyl alcohol. Then, a 2 mL aliquot of the solution was removed from the post-electrolysis electrolyte after the reaction. Subsequently, 2 mL color reagent was added to the above product extract. The absorption spectra of the mixed solution were measured with an ultraviolet-visible spectrophotometer. The concentration of N₂H₄ was determined by absorbance at a wavelength of ~458 nm. The concentration of N₂H₄ were determined by a standard curve (Absorbance = 0.13254 × C_{N₂H₄} - 0.03875, R² = 0.998).

2.6. Isotope labeling static experiments and in situ characterizations

Isotope labeling static experiments used ¹⁵N₂ as feeding gas were conducted to clarify the source of ammonia. The reactor was previously encapsulated and degassed with argon several times, and subsequently filled with ¹⁵N₂. After the NRR procedure, the obtained ¹⁵NH₄⁺ electrolyte (0.1 mL, concentrated electrolyte) was thoroughly mixed with 0.5 mL dimethyl sulphoxide-D6 and 0.1 mL D₂O for the 1 H nuclear magnetic resonance (NMR) test on a Bruker Avance spectrometer (500 MHz). For comparison, the ¹⁴N₂ experiment was also operated in the same way.

The in situ Raman characterizations were conducted using tailor-made cell. Ag/AgCl (saturated KCl) and platinum sheet were used as the reference and counter electrodes, respectively. The electrolyte (0.05 M Na₂SO₄) was saturated with purified N₂ before testing. For in situ Raman measurements, the chronoamperometric tests were conducted using a CHI760E electrochemical workstation (Shanghai Chenhua Instrument Co.) under -0.1 V versus RHE, and the in situ Raman spectra were collected using an inVia Reflex (Renishaw, UK) system.

2.7. Density functional theory (DFT) calculations details

All the spin theoretical simulations in our work were carried out on the Vienna ab initio Simulation Package (VASP) with version 5.4.1 [47]. The Generalized gradient approximation (GGA) with the Perdew-Burke-Ernzerhof (PBE) [48] functional form was employed to evaluate the electron-electron exchange and correlation interactions while the projector augmented-wave (PAW) [49] methods were implanted to represent the core-electron (valence electron) interactions. Plane-Wave basis function was set with a kinetic cut-off energy of 500 eV. A Monkhorst-Pack meshe [50] with the size of 5 × 5 × 1 were employed to sample surface Brillouin zone. The ground-state atomic geometries were optimized by relaxing the force below 0.02 eV/Å and the convergence criteria for energy was set with the value of 1.0 × 10⁻⁵ eV/cell. In order to conduct accurate calculations of electronic structure and total energy, the Gaussian method was employed. Van der Waal (vdw) interactions are included describing by the DFT-D3 method of Grimme [51], to obtain a better description of the interactions between molecules. The 3 × 2 Mo₂C (100) and Rh-Mo₂C (100) were employed for our simulations with C-terminated. The bottom atom-layer was fully relaxed while the bottom layer was fixed during geometries optimization. Free Energy under standard conditions (298 K) was calculated. Gibbs free Energy (ΔG) is computed by the equation of ΔG = ΔE + ΔE_{ZPE} - TΔS, where the ΔE is the difference energy between each reaction step, ΔE_{ZPE} is the difference of the zero-point energy between each reaction step, ΔS is the difference of vibrational entropy between

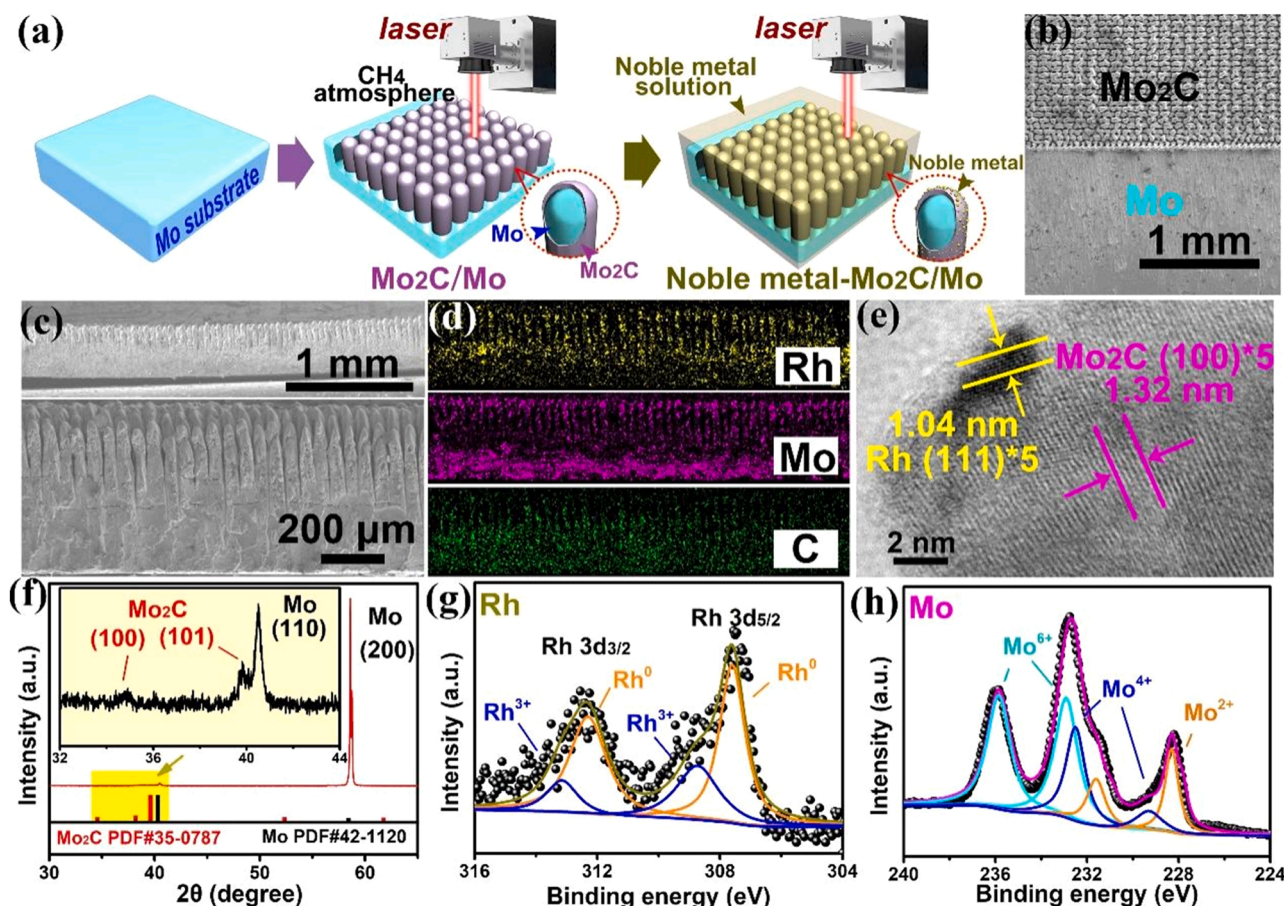


Fig. 1. (a) Schematic illustration of the laser-tuning strategy for the formation of M-Mo₂C. (b-c) Front- and side-view SEM images, (d) Side-view EDS elemental mappings, (e) HRTEM image, (f) XRD pattern, and (g-h) Rh 3d and Mo 3d XPS profiles of Rh-Mo₂C.

each reaction step.

3. Results and discussion

3.1. Catalyst characterizations

Utilizing the energy localization and thermal effect of lasers, M-Mo₂C (M = Ru, Rh, Pd, Ir, Pt) microrod arrays on Mo electrodes were synthesized via a two-step method (Fig. 1a and Fig. S1, Supporting Information). The precursor was laser scanned to convert the Mo substrates into Mo₂C micro-pillars under CH₄ atmosphere (pulsed laser ablation in the atmosphere, PLAA). Then, the prepared Mo₂C/Mo target was further processed by pulsed laser ablation in liquid (PLAL). The noble-metal solution was heated by a pulsed laser to a plasma or vapor state and quenched by the cool water to a solid state. Morphological characterization demonstrates that the micro-pillar structure of Rh-Mo₂C is well preserved after PLAL and maintains an average length and lateral dimension of 400 μm and 20 × 40 μm, respectively (Fig. 1b-c and Fig. S2, Supporting Information). The energy-dispersive spectroscopy (EDS) elemental mappings verify the uniform distribution of Rh, Mo and C (Fig. 1d and Table S1, Supporting Information). The ICP-MS results further confirmed the loading amount of Rh is 160 μg cm⁻² (Table S2, Supporting information). Moreover, the corresponding high-resolution transmission electron microscopy (HRTEM) image shows that Rh nanoparticles are embedded on Mo₂C (Fig. 1e). The interplanar spacing of the embedded Rh nanoparticles is ~2.16 Å, which corresponds to the (111) facets of Rh. Surrounding the nanoparticles is a preserved highly crystalline structure with lattice fringe spaces of 2.60 Å, which corresponds to the (100) facets of Mo₂C.

X-ray diffraction (XRD) was performed to investigate the characteristic structure of Rh-Mo₂C. In addition to the characteristic peaks of Mo, the diffraction pattern shows peaks assignable to the standard Mo₂C (JCPDS card No. 35-0787), indicating that Mo₂C was successfully synthesized by PLAA (Fig. 1f). No Rh peaks were detected due to the low loading amount of Rh. In addition, X-ray photoelectron spectroscopy (XPS) and X-ray absorption near-edge structure (XANES) spectroscopy were performed to analyze the valence state and local electronic structure of Rh-Mo₂C (Figs. S3-5, Supporting Information). As shown in the Rh 3d XPS profile (Fig. 1g), Rh-Mo₂C has typical peaks for Rh⁰ at 307.6 and 312.2 eV, which are ascribed to the Rh 3d_{5/2} and Rh 3d_{3/2} states, respectively [52]. Furthermore, Rh³⁺ presents two prominent peaks at 308.7 and 313.2 eV. Indexing the Mo 3d spectrum (Fig. 1h) reveals three Mo species: Mo²⁺ (228.3 and 231.6 eV), Mo⁴⁺ (229.3 and 232.5 eV), and Mo⁶⁺ (232.9 and 235.85 eV) [36,37]. The coupling of Rh and Mo²⁺ is thought to be active for NRR, whereas the presence of Rh³⁺, Mo⁴⁺ and Mo⁶⁺ species can be explained by the surface oxidation of Rh-Mo₂C.

The XANES spectra revealed that the Mo K-edge position of Rh-Mo₂C is located between that of the Mo foil and Mo₂C, indicating the positive valence state of Mo, owing to the electronic interaction between Rh and Mo₂C upon hybridization (Fig. 2a and Fig. S4, Supporting Information). The adsorption energy decreases in the order: Mo₂C > Rh-Mo₂C > Mo foil, indicating a decrease in the Mo valence state. Furthermore, Fourier-transformed extended X-ray absorption fine structure (FT-EXAFS) spectra were measured to investigate the change in the coordination structure of Rh-Mo₂C relative to the Mo₂C and Mo foil controls (Fig. 2b). The Mo-Mo contribution scattering is slightly shifted in Rh-Mo₂C and Mo₂C (2.66 Å) compared with that in the Mo foil (2.42 Å), indicating the characteristic Mo-Mo1 coordination of Mo₂C. The peak assigned to the

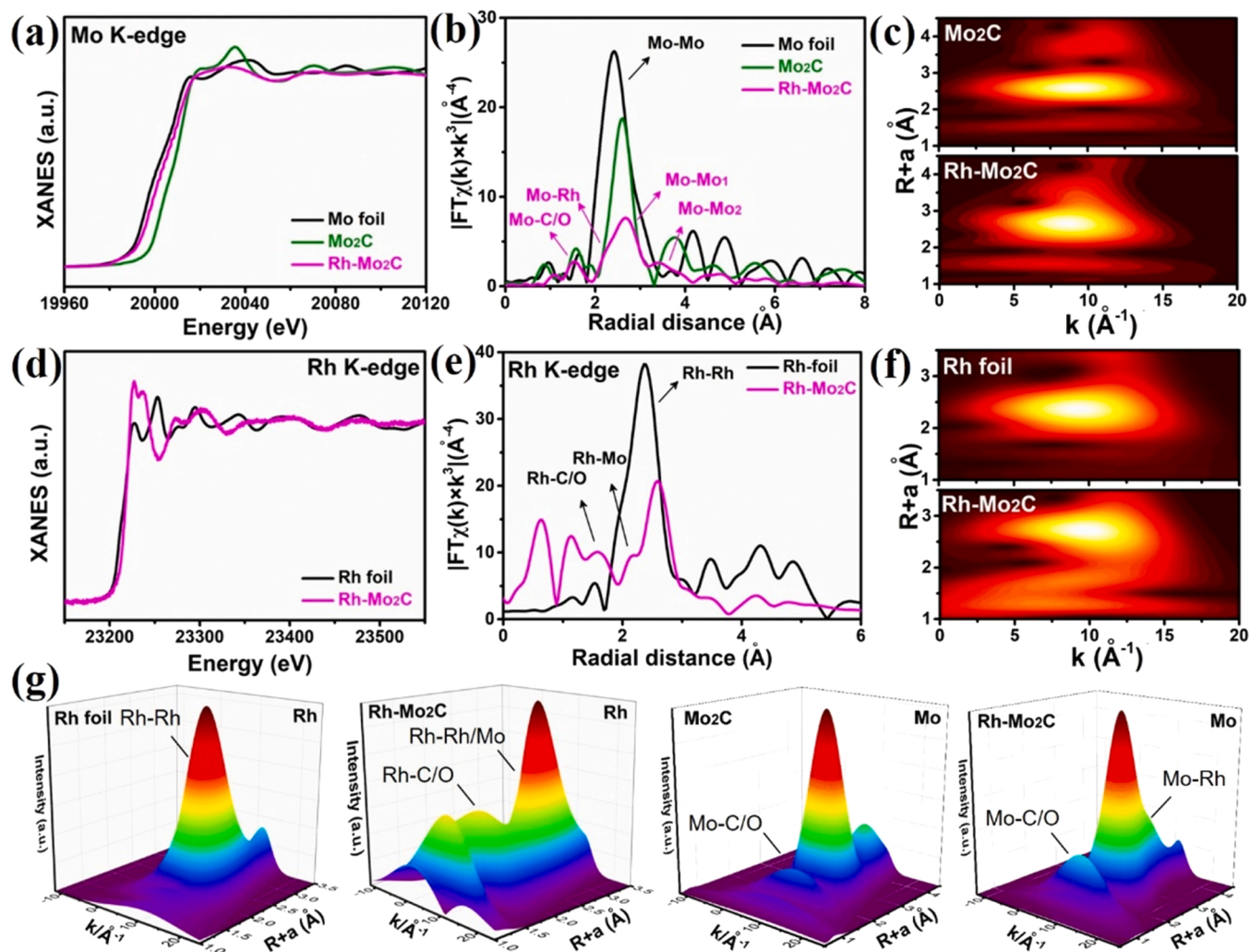


Fig. 2. (a) Normalized XANES spectra at the Mo K-edge of Rh-Mo₂C, Mo₂C and Mo foil. (b) FT-EXAFS spectra derived from EXAFS at the Mo K-edge. (c) Wavelet transforms for the k₃-weighted Mo K-edge EXAFS signals of Mo₂C and Rh-Mo₂C. (d) Normalized XANES spectra at the Rh K-edge of Rh-Mo₂C and Rh foil. (e) FT-EXAFS spectra derived from EXAFS at the Rh K-edge. (f) Wavelet transforms for the k₃-weighted Rh K-edge EXAFS signals of Rh foil and Rh-Mo₂C. (g) The 3D view of wavelet transforms for the k₃-weighted Rh/Mo K-edge EXAFS signals.

Mo-C(O) contribution (1.55 Å) is shifted lower by 0.02 Å compared to that of Mo₂C. Moreover, the existence of the Mo-Rh bond (2.26 Å) and Mo-Mo2 bond (3.69 Å) further confirms the successful embedding of Rh atoms and the slight increase in the Mo valence state, which may be conducive to increasing the availability of the outermost Mo orbital for the adsorption of nitrogen lone pair electrons. The coordination configuration in Rh-Mo₂C has two characteristic paths: Mo-Mo1, Mo-Mo2 and Mo-C. Moreover, an intensity maximum at a higher K-space of 12 Å⁻¹ occurs in Rh-Mo₂C, which arises from the Mo-Rh path (Fig. 2c). The Rh K-edge XANES and FT-EXAFS spectra of Rh-Mo₂C and Rh foil confirm the chemical bonding between Rh and Mo/C (Fig. 2d-e and Fig. S5, Supporting Information). The FT-EXAFS spectra illustrate that Rh-Mo₂C is still dominated by metal coordination, consistent with the previously discussed structural characterizations (Fig. 2b). The peaks located at 2.15 and 1.14 Å are assigned to Rh-Mo and Rh-C coordination, respectively. Moreover, EXAFS wavelet transform (WT) analysis investigated the atomic dispersion by providing both the K-space and radial distance resolution (Fig. 2f). The WT contour plots for both Rh foil and Rh-Mo₂C display intensity maximums at ~10 Å⁻¹, indicating the dominant Rh-metal (Rh-Rh) coordination with notable Rh-Mo/C/O coordination during the preparation process (Fig. 2g). These results verify that the Rh sites cause structural distortion of Mo₂C. The detailed structural parameters are summarized from the curve fitting in Table S3-

4, Supporting Information. Rh-Mo₂C with an optimal *eg*₁ electron configuration and increased Mo⁶⁺ content significantly promotes π back-donation, which further enhances NRR performance.

3.2. Feasibility and mechanism analysis of nitrogen fixation

Furthermore, N₂-temperature-programmed desorption (TPD) was performed to accurately quantify the potential of Rh-Mo₂C for NRR (Fig. 3a) [53]. The peaks located at 357 °C indicate that Rh-Mo₂C possesses more moderate-to-strong acid sites than Mo₂C. Similar phenomenon occurred in NH₃-TPD tests further confirmed that the synthesized Mo₂C shows a notable Lewis acid character after the introduction of Rh (Fig. S6, Supporting Information). The Lewis acid sites could capture N₂ (Lewis base) with lone pair electrons and activate N≡N bonds [29]. First-principles density functional theory (DFT) calculations and the free energies of critical NRR steps were used to further discern the influence of electronic structure on the NRR activity of Rh-Mo₂C (Fig. S7, Supporting Information). The density of states (DOS) in Fig. 3b-c show that the C-2p and Mo-3d orbitals in Mo₂C have strong hybridization, while the Rh-3d orbitals have noticeable overlap with C-2p around the Fermi level in Rh-Mo₂C. This suggests efficient Rh 3d and C 2p coupling and electron transferring owing to the maintainable Rh sites with lower valence states. Relative to Mo₂C, the slightly delocalized DOS in

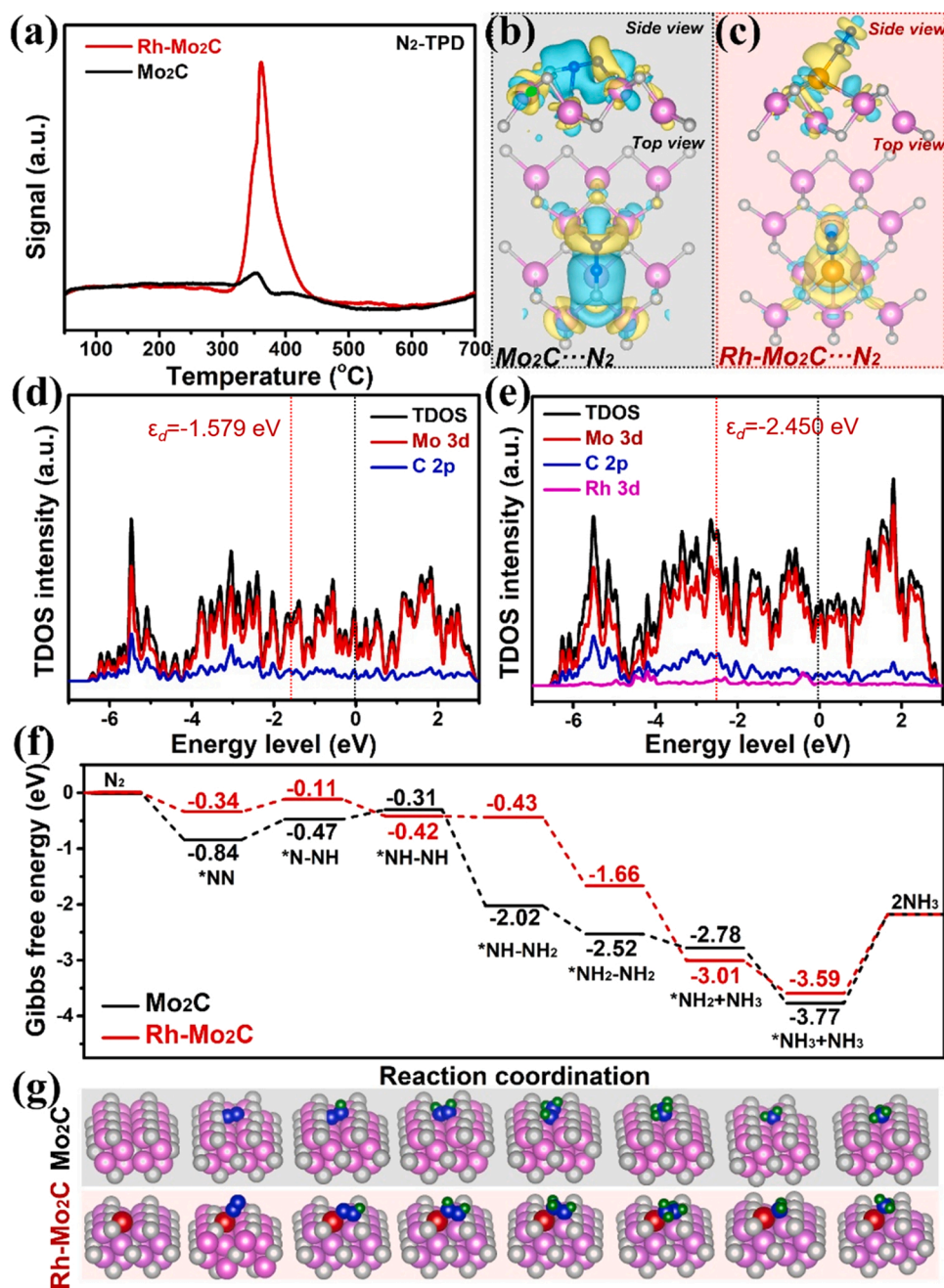
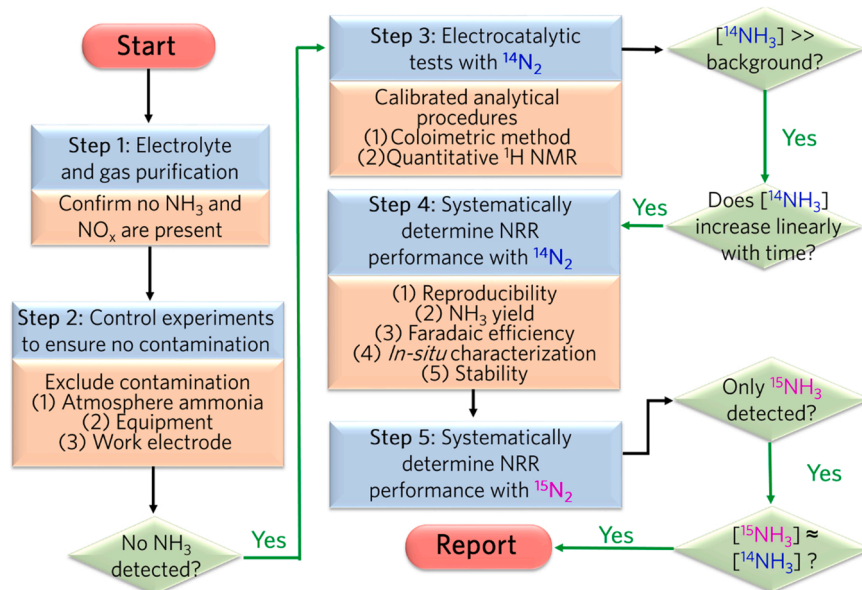


Fig. 3. (a) N₂-TPD patterns of Mo₂C and Rh-Mo₂C. (b-c) Side- and top-views of the charge density differences of the optimized Mo₂C/Rh-Mo₂C...N₂ and Mo₂C/Rh-Mo₂C...NH₃ structures. Blue and yellow regions represent electron depletion and accumulation, respectively. (d-e) Calculated projected density of states (PDOS) of Mo₂C and Rh-Mo₂C with the aligned Fermi levels set to 0 eV. The labeled ϵ_d is the d-band centers of Mo and Rh, respectively. (f) Calculated free energy diagram of the NRR mechanism on Mo₂C and Rh-Mo₂C. (g) The optimized structures of intermediate adsorption on Mo₂C and Rh-Mo₂C. The pink, gray, red, green, and blue represent Mo, C, Rh, H and N atoms, respectively.

Rh-Mo₂C near the Fermi level also directly enhances the electronic conductivity. Furthermore, the charge density difference calculations and Bader charges show that more electrons can be donated to the *N₂ species from Rh sites, thus promoting activation of *N₂ in Rh-Mo₂C (Fig. 3d-e and Fig. S8-9, Supporting information). The *d*-band center of Mo on Mo₂C located at -1.579 eV and the parameter of Rh on Rh-Mo₂C is -2.450 eV. Mo on Mo₂C achieves a shallower *d*-band center, resulting in unfavorably strong binding of NRR intermediates and high reaction energy barriers. In contrast, Rh on Rh-Mo₂C induces a deeper *d*-band center. Consequently, the binding of the intermediates on Rh-Mo₂C are weakened, lowering energy barriers of hydrogenation process and enhancing the NRR activity. Moreover, the strong adsorption ability of Rh-Mo₂C can be explained by the hybridized Rh-3*d* orbitals. These orbitals promote electron back-donation to the antibonding π^* -orbitals of N₂ and charge transfer from Rh to the N-2*p* orbital, forming the NN* adsorption species [54]. Furthermore, NH₃ desorption occurs more

readily in Rh-Mo₂C than Mo₂C. Meanwhile, the bond length of Rh-Mo₂₀ is 2.69 Å, which is similar to that of Rh-Mo₂₈ (2.70 Å) (Fig. S10, Supporting Information). Rh loses 0.08 electrons, C₅₂ and C₅₅ in the immediate vicinity of Mo₂₀ also lose electrons, and these above electrons are transferred to Mo₂₀. Mo₂₈ loses 2.15 electrons and these electrons transfer to Rh. Hence, Rh sites embedded on Mo₂C function as the primary catalytic sites and electron back-donating centers for N₂ adsorption and activation.

Accordingly, the N₂ adsorption and activation behaviors along the proposed NRR pathway on Rh-Mo₂C and Mo₂C were investigated to elucidate the complete NRR mechanism. The basic mechanisms for N₂-to-NH₃ conversion can be classified into three types, including dissociative, associative pathways and enzymatic pathway [8]. The initial adsorption configuration influences the subsequent NRR pathway. Considering that the complete fracture of nitrogen in the first step requires huge energy, the dissociative pathway mostly occurs in the



Scheme 2. The experimental protocol for reliable proof of electrochemical nitrogen reduction reaction.

Haber-Bosch process proceeds. Associative pathways and enzymatic pathway are the optimal selection with lower energy barrier for electrocatalysis. Meanwhile, the model of bi-dentate adsorption on Rh-Mo₂C system is not stable, and the subsequent enzymatic pathway theoretical calculation cannot be carried out (Fig. S11 and Table S5, Supporting information). The associative alternating pathway and associative distal pathway were both explored (Fig. S12, Supporting information). For Rh-Mo₂C, the hydrogenation step $^*N(-NH_3) \rightarrow ^*NH(-NH_3)$ in distal pathway is one of the main rate-determining steps with energy barrier (2.06 eV), which is higher than that of alternating pathway. Therefore, the preferable pathway on active sites is $N_2 \rightarrow ^*N-N \rightarrow ^*N-NH \rightarrow ^*NH-NH \rightarrow ^*NH-NH_2 \rightarrow ^*NH_2-NH_2 \rightarrow ^*NH_2-NH_3 \rightarrow ^*NH_3-NH_3 \rightarrow 2NH_3$. As illustrated in Fig. 3f-g, hydrogenation ($^*NN \rightarrow ^*N-NH$) and NH₃

dissociation are the two main rate-determining steps. A good catalyst should neither be too strong nor too weak in its adsorption of intermediate species. The strong binding of N₂ on Mo₂C results in a higher energy barrier of the first step ($^*NN \rightarrow ^*N-NH$). However, the free energy of the initial N₂ adsorption on Rh-Mo₂C is moderate, which reduces the $^*NN \rightarrow ^*N-NH$ energy barrier. The last dissociation step of Rh-Mo₂C has the highest energy barrier (−3.59 eV) and is the rate-limiting step, which can be overcome by the accumulation of free energy in previous reaction processes. Moreover, the $^*NH-NH \rightarrow ^*NH-NH_2$ energy barrier of Rh-Mo₂C is notably lower than that of Mo₂C, which facilitates NRR after the introduction of Rh (Fig. S13, Supporting Information). Therefore, the rational regulation of the interfacial microstructure of Mo₂C by introducing Rh heteroatoms exposes more active sites for N₂ activation,

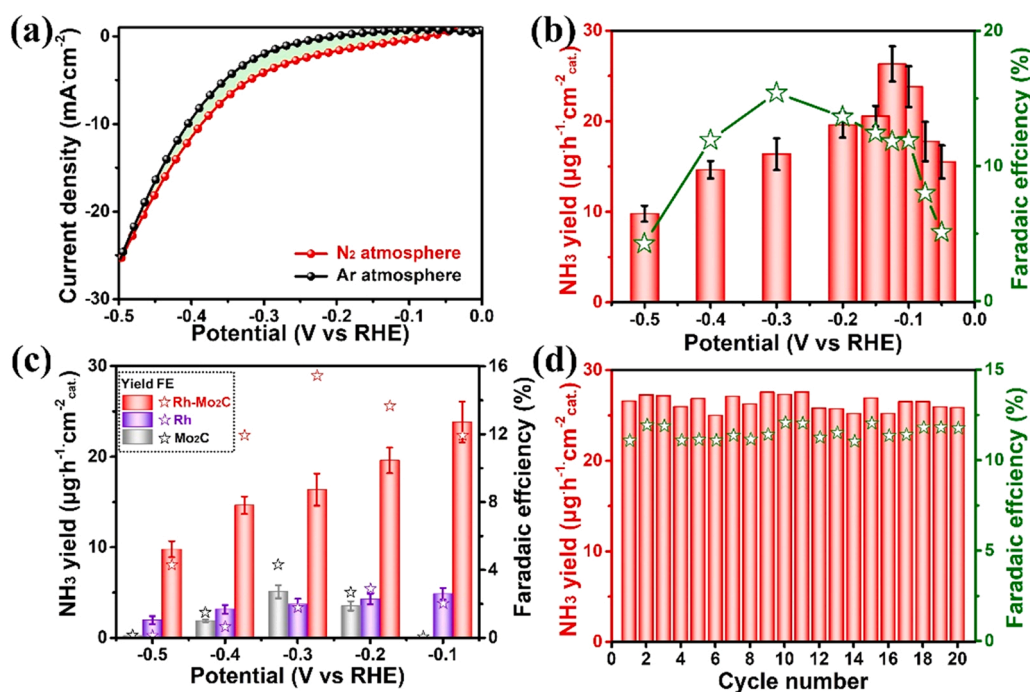


Fig. 4. (a) Linear-sweep voltammetric curves of Rh-Mo₂C in Ar- and N₂-saturated electrolyte. (b-c) NH₃ yields and Faradaic efficiencies of Rh-Mo₂C and control samples for NRR at various potentials. (d) NH₃ yields and Faradaic efficiencies of Rh-Mo₂C at a potential of −0.125 V vs. RHE over 20 cycles.

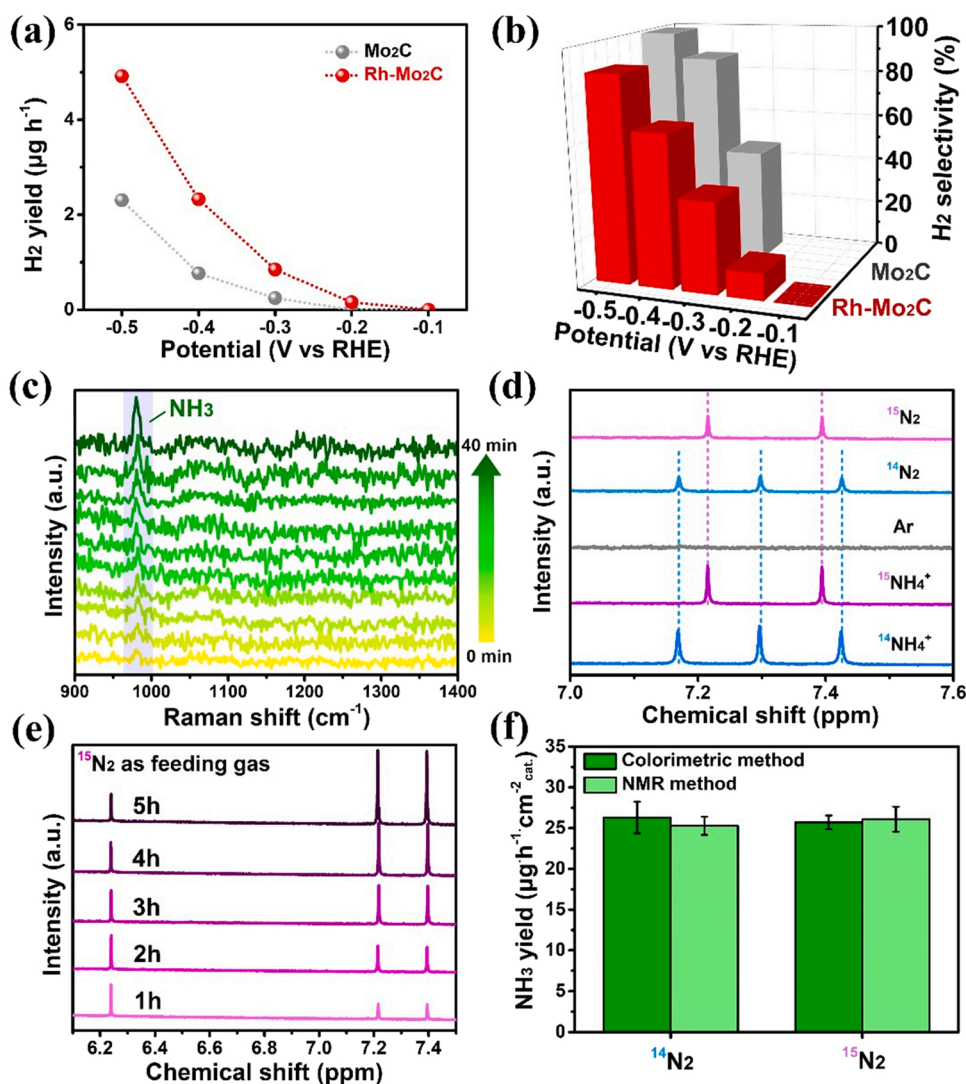


Fig. 5. (a) H₂ yields of Mo₂C and Rh-Mo₂C. (b) The inset shows H₂ selectivity of different electrodes. (c) in situ Raman spectra of Rh-Mo₂C collected at -0.125 V versus RHE under N₂ atmosphere. (d) ¹H NMR spectra of both ¹⁴NH₄⁺ and ¹⁵NH₄⁺ obtained from the NRR on Rh-Mo₂C using ¹⁴N₂ or ¹⁵N₂ as the nitrogen source, respectively. (e) ¹H NMR spectra of the electrolyte with different electrolysis times under ¹⁵N₂ atmosphere. (f) Calculated NH₃ yield rates at -0.125 V versus RHE using colorimetric and NMR quantification methods. The error bars correspond to the standard deviations (n = 3) of measurements taken under the same conditions.

modifies the surface chemical states and optimizes the migration path of hydrogen.

3.3. Nitrogen fixation catalytic activity and selectivity

Intriguingly, the theoretical calculations suggest that the engineered interfacial microstructure with Lewis acid sites could mimic π back-donation behavior on Rh-Mo₂C and enhance electrochemical NRR. Meticulous control experiments including ¹⁵N₂ isotope labelling and in-situ characterization were carried out to verify that NH₃ was indeed produced by the electrochemical NRR over Rh-Mo₂C and not by a contaminant (Scheme 2). Prior to entering the cell, the feeding gas was purified by an H₂SO₄ solution to remove any remaining contaminants, such as NH₃ and NO_x (Fig. S14, Supporting Information) [55]. The N₂ gas supply was also sufficiently purified to remove possible contaminants (Fig. S15, Supporting Information). Linear-sweep voltammetry (LSV) curves of Rh-Mo₂C in both Ar- and N₂-saturated 0.05 M Na₂SO₄ electrolytes are shown in Fig. 4a. The LSV curve obtained with N₂ bubbling shows a higher current in the potential range of -0.10 to -0.50 V vs. RHE, where NRR is favored, attesting to the efficiency of NRR on Rh-Mo₂C. In addition, the chronoamperometry curves show that the current density at various potentials remains stable over a 3 h period (Fig. S16, Supporting Information). The corresponding UV-vis absorption spectra illustrate that the maximum absorbance occurs at -0.125 V (Fig. S17, Supporting Information). The absorption intensities of the

electrolytes following Rh-Mo₂C-catalyzed NRR are much higher than those of the Rh and Mo₂C controls over the tested potential range (Fig. S18-19, Supporting Information). Rh-Mo₂C achieved a high NH₃ yield rate of 26.3 μg h⁻¹ cm⁻² cat. (4.30×10^{-10} mol s⁻¹ cm⁻² cat.) at -0.125 V and a Faradic efficiency (FE) of 15.4% at -0.3 V, which are approximately 5.1- and 3.6-fold higher than those of Mo₂C, respectively (Fig. 4b-c, and Fig. S20, Supporting Information). Meanwhile, the NRR performance of Rh-Mo₂C is also superior to several published representative work (Table S6, Supporting Information). The NH₃ yield notably decreases beyond the favorable NRR potential range. This decrease is attributed to an increase in the competitive adsorption of hydrogen and nitrogen intermediate species on the catalyst surface. These results show that Rh-Mo₂C has an increased capacity for nitrogen activation. Furthermore, electrochemical impedance spectroscopy (EIS) plots show semicircles characteristic of Warburg impedance (Fig. S21, Supporting Information). Rh-Mo₂C shows lower charge transfer resistance (R_{ct}) than Mo₂C at the favorable NRR potential of -0.125 V, suggesting fast reaction kinetics and rapid electron transfer.

Furthermore, the chronoamperometry curves show a negligible change in the current density after 20 consecutive cycles, confirming the strong electrochemical stability of Rh-Mo₂C (Fig. S22, Supporting Information). Moreover, no notable fluctuations in the NH₃ yield and FE are observed after a continuous 60 h long-term process (20 cycles), attesting to the robust NH₃ synthesis and excellent structural stability of Rh-Mo₂C (Fig. 4d). SEM images under different magnifications show

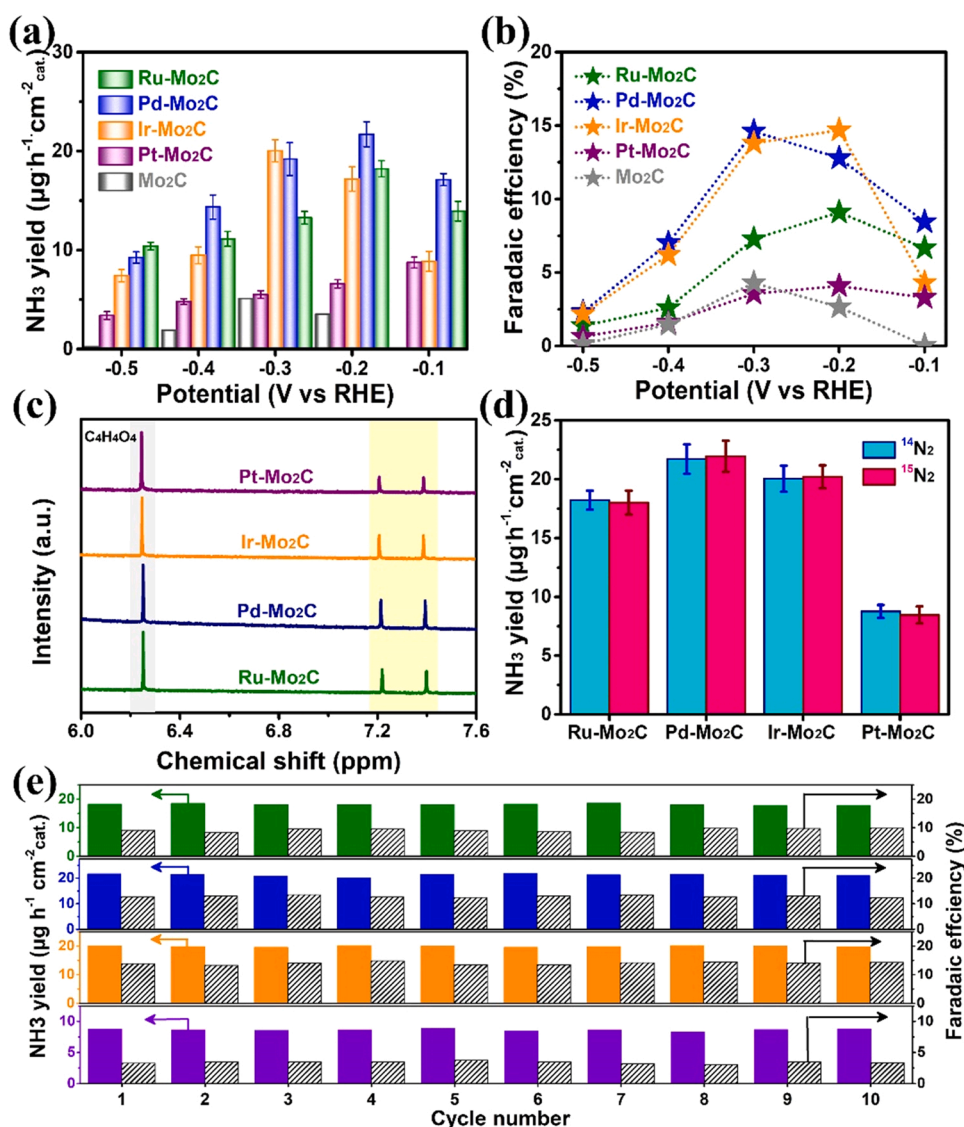


Fig. 6. (a) NH₃ yields and (b) Faradaic efficiencies of M-Mo₂C (M = Ru, Pd, Ir, Pt) for NRR performance. (c) ¹H NMR spectra of M-Mo₂C (M = Ru, Pd, Ir, Pt) at the respective optimized work potential. (d) Comparison of the calculated NH₃ yield rates using different quantification methods for the M-Mo₂C (M = Ru, Pd, Ir, Pt) catalyzed system. The error bars correspond to the standard deviations of triplicate sample measurements under the same conditions. (e) NH₃ yields and Faradaic efficiencies of M-Mo₂C at optimized potential over 10-time cycles. The olive, blue, orange and purple represent Ru-Mo₂C, Pd-Mo₂C, Ir-Mo₂C and Pt-Mo₂C, respectively.

that the morphology is nearly unchanged following a durability test (Fig. S23, Supporting Information). To further verify the stability, XPS was again employed to explore the possible changes in the characteristic structure and valence state of Rh-Mo₂C after NRR (Fig. S24, Supporting Information). The Rh 3d spectrum shows negligible changes in the Rh 3d_{5/2} and Rh 3d_{3/2} peaks at 307.7 and 312.2 eV for Rh⁰, respectively. The high-resolution XPS profiles of Mo 3d and C1s show no shift in the typical peaks for Mo²⁺ and C-based bonds after long-term NRR stability tests. However, the peaks for Mo^{2+/4/6+} 3d_{5/2} and Mo^{2+/4/6+} 3d_{3/2} are slightly shifted in the negative direction after the electrochemical measurements, and the Mo²⁺/Mo^{4/6+} ratio increased, which could be ascribed to the slow dissolution and partial reduction of high-valence molybdenum at low operating potentials [36,37]. This slight change has no impact on the overall structural stability of materials. Overall, Rh-Mo₂C shows excellent electrochemical durability and structural stability.

Further investigations of the HER performance provided additional evidence that the introduction of Lewis acid sites effectively provide more active hydrogen and can suppress the strong HER to make the NRR reaction on Mo₂C more selective (Fig. 5a). Hydrogen selectivity is greatly reduced at low voltage, which confirm the ammonia selectivity at optimized work potential (Fig. 5b). In addition, the formation of the hydrazine by-product was monitored. At the optimum voltage, the

hydrazine yield on Rh-Mo₂C is negligible, which indicates excellent selectivity towards NRR (Fig. S25-26, Supporting Information). In situ tests and isotope labelling experiments with purified ¹⁵N₂ gas (Fig. S27, Supporting Information) were performed to confirm that the produced NH₃ was solely derived from the supplied N₂ [9,56]. In situ Raman spectroscopy were used to monitor products (NH₃) under the potentiostatic operation (Fig. S28, Supporting information). The Raman peak at ~982, assigned to NH₃ [9], gradually appeared for Rh-Mo₂C as the reaction progressed, indicating the occurrence of NRR on the electrode surface (Fig. 5c). Meanwhile, Ar was acted as the feeding gas before isotope labelling experiments. As expected, no peaks are detected in the ¹H NMR spectra (Fig. 5d). Commercial ¹⁴NH₄Cl and ¹⁵NH₄Cl samples were used as standards. When the feeding gas was changed to ¹⁴N₂, a triple peak signal for ¹⁴NH₄⁺ with ~52.4 Hz spacing is detected, which is in close agreement with the reference substance of ¹⁴NH₄Cl. In particular, the ¹H NMR spectra exhibit a ¹⁵N doublet (I = 1/2, δ 6.8–7.1 ppm) with ~72.8 Hz spacing, while the ¹⁴N triplet is not observed [57,58]. These results demonstrate that the detected NH₃ is completely derived from the supplied N₂. The amount of accumulated NH₃ is linearly correlated with the reaction time with either ¹⁴N₂ or ¹⁵N₂ as feeding gas (Fig. 5e and S29–32, Supporting Information). Additionally, there is a near-negligible difference in the NH₃ yield at -0.125 V versus RHE under ¹⁵N₂ or ¹⁴N₂ atmosphere using both the

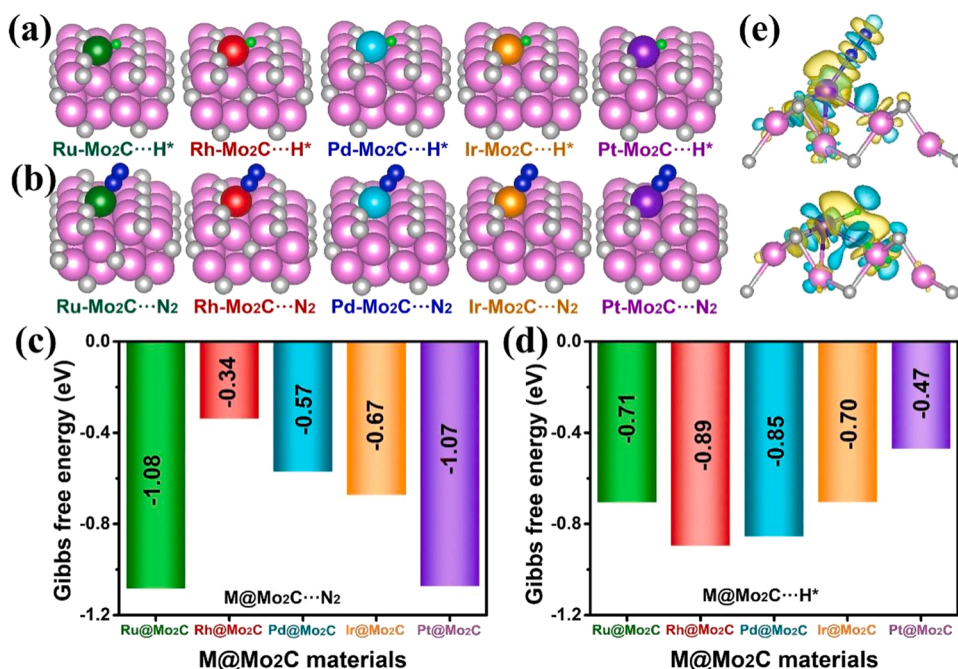


Fig. 7. (a-b) Optimized structures of intermediate H* and N₂ adsorption on M-Mo₂C (M = Ru, Pd, Ir, Pt). The pink, gray, olive, red, cyan, orange, purple, green and blue represent Mo, C, Ru, Rh, Pd, Ir, Pt, H and N atoms, respectively. DFT-calculated adsorption energies of N₂ (c) and H* (d) on M-Mo₂C (M = Ru, Pd, Ir, Pt). (e) Side-view of the charge density difference of the optimized structure of Pt-Mo₂C...N₂ and Pt-Mo₂C...H*. Blue and yellow regions represent electron depletion and accumulation, respectively.

NMR and colorimetric method, further demonstrating the reliability of the obtained NRR results (Fig. 5f).

3.4. Universal mechanism of laser tuning for Lewis acid sites

To verify the universality of the optimized microstructure mimicking π back-donation, a family of M-Mo₂C (M = Ru, Pd, Ir, Pt) materials were synthesized via a general laser-tuning strategy. Similar to Rh-Mo₂C, the micro-pillar morphology of M-Mo₂C was well preserved with a uniform distribution of corresponding elements (Fig. S33–34, Supporting Information). The corresponding structural characterization, surface chemical composition and bonding configuration results further confirmed the successful preparation of Mo₂C embedded with different noble metals (Fig. S35–36, Supporting Information). The loading amount of noble metals range from 146 to 183 $\mu\text{g cm}^{-2}$, which is similar to that of rhodium (Table S2, Supporting Information). Each noble metal and Mo₂C heterojunction demonstrated the successful tuning of the interfacial microstructure. In addition, the difference in work function between the noble metals (Ru, 4.71 eV; Rh, 4.98 eV; Pd, 5.12 eV; Ir, 5.27 eV; Pt, 5.56 eV) and Mo₂C (5.00 eV) induced the charge redistribution across the interfacial microstructure and further promoted electron transfer between the noble metals and Mo₂C [59,60].

The catalytic performances of M-Mo₂C (M = Ru, Pd, Ir, Pt) for NRR were investigated under the same conditions. The strategy of laser tuning the interfacial microstructure of Rh-Mo₂C for improved NRR catalytic properties was found to be extendable to other noble metals. Fig. S37 in the Supporting Information exhibits the LSV curves of the synthesized M-Mo₂C materials in Ar- and N₂-saturated electrolyte. Ru-Mo₂C exhibits a higher current at a potential of -0.3 V vs. RHE in N₂-saturated solution, while the others have onset potentials at -0.1 V vs. RHE. The chronoamperometry and UV-vis absorption spectra were measured to quantify the NH₃ yield (Fig. S38–S39, Supporting Information). The FE for the as-synthesized catalysts are summarized in Fig. 6a–b. The maximum NH₃ yield of M-Mo₂C (M = Ru, Pd, Ir) ranged between 18.2 and 21.7 $\mu\text{g h}^{-1} \text{cm}_{\text{cat}}^{-2}$, which is approximately 3- to 4-fold higher than that of Mo₂C. The same trend is observed for FE; M-Mo₂C (M = Ru, Pd, Ir) measured FEs were 9.1%, 14.6%, and 14.7%, respectively, higher than that of Mo₂C (4.3%). However, Pt-Mo₂C exhibits unsatisfactory activity with an NH₃ yield (8.8 $\mu\text{g h}^{-1} \text{cm}_{\text{cat}}^{-2}$ at -0.1 V) and FE

(4.2% at -0.2 V) that are considerably inferior to those of M-Mo₂C (M = Ru, Rh, Pd, Ir). This can be explained by the dominance of the HER on Pt-Mo₂C and demonstrated the importance of selecting an appropriate noble metal for promoting N₂ fixation. Furthermore, EIS plots of M-Mo₂C showed semicircles characteristic of Warburg impedance (Fig. S40, Supporting Information). M-Mo₂C (M = Ru, Pd, Ir, Pt) exhibited lower charge transfer resistance (R_{ct}) than Mo₂C at the favorable NRR potential, suggesting fast reaction kinetics and rapid electron transfer.

As is the case for Rh-Mo₂C, ¹⁵N isotope labelling experiments confirm that the produced NH₃ is derived entirely from the supplied N₂ for all the synthesized catalysts. The ¹H NMR spectra show a ¹⁵N doublet ($I = 1/2$) with ~ 73 Hz spacing, while a distinct ¹⁴N triplet is absent (Fig. 6c) [61–63]. There is no notable difference in the NH₃ yield under a ¹⁵N₂ and ¹⁴N₂ atmosphere for the M-Mo₂C-catalyzed system (M = Ru, Pd, Ir, Pt, Fig. 6d). After a continuous 30 h long-term test, the chronoamperometry curves for M-Mo₂C all show no notable decrease in current density, verifying the high electrochemical stability of the catalysts (Fig. S41, Supporting Information). Furthermore, the NH₃ yield and FE of M-Mo₂C are effectively maintained over ten consecutive cycles, which demonstrates the outstanding catalytic stability of this material system (Fig. 6e).

The structure-activity relationship between the noble-metal active sites and NRR activity was investigated by theoretical calculations. Introducing noble-metal Lewis acid sites that mimic π back-donation can effectively improve the N₂ adsorption and activation capacity. However, considering that noble metals are very good proton activation sites, proton generation in large quantities may result in the enrichment of active hydrogen and thus, favor HER. The active hydrogen- and nitrogen-adsorption energies of M-Mo₂C (M = Ru, Rh, Pd, Ir, Pt) are different. Considering the whole reaction path, the adsorption energy of the active site for different intermediates is correlated which adds up to a constant value (Fig. 7a–b and Fig. S42, Supporting Information). The adsorption of an intermediate at the active site should not be too weak or too strong; an optimal adsorption value should be maintained near 0. Therefore, Rh-Mo₂C has the best nitrogen adsorption energy, while Pt-Mo₂C has better active hydrogen adsorption energy (Fig. 7c). The charge density difference calculations of Pt-Mo₂C further show that more electrons could be donated to the *N₂ species from Pt sites (Fig. 7d–e).

However, the excellent active hydrogen adsorption capacity increases the HER side reaction, which is consistent with the above NRR activity. In summary, promoting N_2 adsorption and activation capacity and optimizing the migration path of active hydrogen on M-Mo₂C both are the key points to improve NRR efficiency, which can be achieved only by taking both above keys into account.

4. Conclusions

Laser-tuned Lewis acid active sites on the interfacial microstructure promote π back-donation in Mo₂C-based electrocatalysts. This is realized via the introduction of electron back-donating centers on Mo₂C, such as Rh-Mo₂C, which achieves an average NH₃ yield of $\sim 26.3 \mu\text{g h}^{-1} \text{cm}^{-2}$ ($4.30 \times 10^{-10} \text{ mol s}^{-1} \text{cm}^{-2}$) and FE of $\sim 15.4\%$ in Na₂SO₄ electrolyte. Superior to pristine Mo₂C, Rh-Mo₂C has sufficient vacant orbitals on its electron back-donating metal centers to effectively break N \equiv N bonds and lower the thermodynamic energy barrier of the hydrogenation and NH₃ desorption steps. This work provides a general and efficient strategy for designing and engineering the active sites and interfacial microstructures of electrocatalysts and highlights the use of laser tuning to accurately manipulate electrocatalytic performance.

CRediT authorship contribution statement

B. Chang and H. F. Yuan synthesized the materials and performed the electrochemical tests; L. L. Li carried out the theoretical DFT calculation and analysed the DFT results with B. Chang and W. J. Zhou; J. Y. Yu, B. Wang, L. L. Zhao and X. Y. Liu assisted with the EXAFS, in-situ Raman, SEM, TEM, XPS and EDX measurements. X. Y. Liu and W. Q. Yu were involved in the electrochemical studies; B. Chang, H. Liu, W. J. Zhou designed this study; B. Chang, X. Y. Liu, S. H. Sun and W. J. Zhou provided the funding support; B. Chang, S. H. Sun, H. Liu and W. J. Zhou prepared this manuscript.

Declaration of Competing Interest

The authors declare that they have no known competing financial interests or personal relationships that could have appeared to influence the work reported in this paper.

Data Availability

Data will be made available on request.

Acknowledgements

B. Chang and H. F. Yuan contributed equally to this work. This work is supported by the National Natural Science Foundation of China (51972147, 52022037), Taishan Scholars Project Special Funds (tsqn201812083), Innovative Team Project of Jinan (2021GXRC019), the Natural Sciences and Engineering Research Council of Canada (NSERC), Natural Science Foundation of Shandong Province (ZR2019YQ20, ZR2021QE011, ZR2021JQ15), China Postdoctoral Science Foundation (2021M701402), Postdoctoral Innovative Talents Support Program of Shandong Province (SDBX2020009) and the Open Project Program of the State Key Laboratory of Photocatalysis on Energy and Environment (SKLPEE-KF202110). The authors thank Beijing Synchrotron Radiation Facility (BL1W1B station) and Shiyanjia Lab (www.shiyanjia.com), China.

Appendix A. Supporting information

Supplementary data associated with this article can be found in the online version at [doi:10.1016/j.apcatb.2022.121777](https://doi.org/10.1016/j.apcatb.2022.121777).

References

- [1] J. Guo, P. Chen, Catalyst: NH₃ as an energy carrier, *Chem* 3 (2017) 709–712, <https://doi.org/10.1016/j.chempr.2017.10.004>.
- [2] P. Wang, F. Chang, W. Gao, J. Guo, G. Wu, T. He, P. Chen, Breaking scaling relations to achieve low-temperature ammonia synthesis through LiH-mediated nitrogen transfer and hydrogenation, *Nat. Chem.* 9 (2017) 64–70, <https://doi.org/10.1038/nchem.2595>.
- [3] P. Mehta, P. Barboun, F.A. Herrera, J. Kim, P. Rumbach, D.B. Go, J.C. Hicks, W. F. Schneider, Overcoming ammonia synthesis scaling relations with plasma-enabled catalysis, *Nat. Catal.* 1 (2018) 269–275, <https://doi.org/10.1038/s41929-018-0045-1>.
- [4] N. Lazowski, M. Chung, K. Williams, M.L. Gala, K. Manthiram, Non-aqueous gas diffusion electrodes for rapid ammonia synthesis from nitrogen and water-splitting-derived hydrogen, *Nat. Catal.* 3 (2020) 463–469, <https://doi.org/10.1038/s41929-020-0455-8>.
- [5] J. Sun, D. Alam, R. Daiyan, H. Masood, T. Zhang, R. Zhou, P.J. Cullen, E.C. Lovell, A. Jalili, R. Amal, A hybrid plasma electrocatalytic process for sustainable ammonia production, *Energy Environ. Sci.* 14 (2021) 865–872, <https://doi.org/10.1039/d0ee03769a>.
- [6] Y. Li, H. Wang, C. Priest, S. Li, P. Xu, G. Wu, Advanced electrocatalysis for energy and environmental sustainability via water and nitrogen reactions, *Adv. Mater.* 33 (2021), 2000381, <https://doi.org/10.1002/adma.202000381>.
- [7] J.B. Pang, B. Chang, H. Liu, W.J. Zhou, Potential of MXene-based heterostructures for energy conversion and storage, *ACS Energy Lett.* 7 (2021) 78–96, <https://doi.org/10.1021/acsenenergylett.1c02132>.
- [8] G. Qing, R. Ghazfar, S.T. Jackowski, F. Habibzadeh, M.M. Ashtiani, C.P. Chen, M. R. Smith, T.W. Hamann, Recent advances and challenges of electrocatalytic N₂ reduction to ammonia, *Chem. Rev.* 120 (2020) 5437–5516, <https://doi.org/10.1021/acs.chemrev.9b00659>.
- [9] S.S. Liu, T. Qian, M.F. Wang, H.Q. Ji, X.W. Shen, C. Wang, C.L. Yan, Proton-filtering covalent organic frameworks with superior nitrogen penetration flux promote ambient ammonia synthesis, *Nat. Catal.* 4 (2021) 322–331, <https://doi.org/10.1038/s41929-021-00599-w>.
- [10] S.D. Minteer, P. Christopher, S. Linic, Recent developments in nitrogen reduction catalysts: a virtual issue, *ACS Energy Lett.* 4 (2018) 163–166, <https://doi.org/10.1021/acsenenergylett.8b02197>.
- [11] W. Guo, K. Zhang, Z. Liang, R. Zou, Q. Xu, Electrochemical nitrogen fixation and utilization: theories, advanced catalyst materials and system design, *Chem. Soc. Rev.* 48 (2019) 5658–5716, <https://doi.org/10.1039/c9cs00159j>.
- [12] L. Du, L. Xing, G. Zhang, X. Liu, D. Rawach, S. Sun, Engineering of electrocatalyst/electrolyte interface for ambient ammonia synthesis, *SusMat* 1 (2021) 150–173, <https://doi.org/10.1002/sus2.7>.
- [13] Y. Yao, J. Wang, U.B. Shahid, M. Gu, H. Wang, H. Li, M. Shao, Electrochemical synthesis of ammonia from nitrogen under mild conditions: Current status and challenges, *Electrochem. Energy Rev.* 3 (2020) 239–270, <https://doi.org/10.1007/s41918-019-00061-3>.
- [14] Z.H. Yan, M.X. Ji, J.X. Xia, H.Y. Zhu, Recent advanced materials for electrochemical and photoelectrochemical synthesis of ammonia from dinitrogen: One step closer to a sustainable energy future, *Adv. Energy Mater.* 10 (2019), 1902020, <https://doi.org/10.1002/aenm.201902020>.
- [15] J. Chen, W. Zhang, H. Li, W. Li, D. Zhao, Recent advances in TiO₂-based catalysts for N₂ reduction reaction, *SusMat* 1 (2021) 174–193, <https://doi.org/10.1002/sus2.13>.
- [16] Y. Zhang, P.C. Lan, K. Martin, S. Ma, Porous frustrated Lewis pair catalysts: advances and perspective, *Chem. Catal.* 2 (2022) 439–457, <https://doi.org/10.1016/j.cheecat.2021.12.001>.
- [17] Q. Yang, W. Xu, S. Gong, G. Zheng, Z. Tian, Y. Wen, L. Peng, L. Zhang, Z. Lu, L. Chen, Atomically dispersed Lewis acid sites boost 2-electron oxygen reduction activity of carbon-based catalysts, *Nat. Commun.* 11 (2020) 5478, <https://doi.org/10.1038/s41467-020-19309-4>.
- [18] B. Chang, L.L. Li, D. Shi, H.H. Jiang, Z.Z. Ai, S.Z. Wang, Y.L. Shao, J.X. Shen, Y. Z. Wu, Y.L. Li, X.P. Hao, Metal-free boron carbonitride with tunable boron Lewis acid sites for enhanced nitrogen electroreduction to ammonia, *Appl. Catal. B Environ.* 283 (2021), 119622, <https://doi.org/10.1016/j.apcatb.2020.119622>.
- [19] X.Y. Li, S. Feng, M. Zhao, C.X. Zhao, X. Chen, B.Q. Li, J.Q. Huang, Q. Zhang, Surface gelation on disulfide electrocatalysts in lithium-sulfur batteries, *Angew. Chem. Int. Ed.* 61 (2022), e202114671, <https://doi.org/10.1002/anie.202114671>.
- [20] Q.C. Wang, Y.P. Lei, D.S. Wang, Y.D. Li, Defect engineering in earth-abundant electrocatalysts for CO₂ and N₂ reduction, *Energy Environ. Sci.* 12 (2019) 1730–1750, <https://doi.org/10.1039/c8ee03781g>.
- [21] X. Yan, D.L. Liu, H.H. Cao, F. Hou, J. Liang, S.X. Dou, Nitrogen reduction to ammonia on atomic-scale active sites under mild conditions, *Small Methods* 3 (2019), 1800501, <https://doi.org/10.1002/smt.201800501>.
- [22] Y. Tanabe, Y. Nishibayashi, Comprehensive insights into synthetic nitrogen fixation assisted by molecular catalysts under ambient or mild conditions, *Chem. Soc. Rev.* 50 (2021) 5201–5242, <https://doi.org/10.1039/d0cs01341b>.
- [23] C.H. Yang, Y.T. Zhu, J. Liu, Y. Qin, H. Wang, H. Liu, Y. Chen, Z. Zhang, W. Hu, Defect engineering for electrochemical nitrogen reduction reaction to ammonia, *Nano Energy* 77 (2020), 105126, <https://doi.org/10.1016/j.nanoen.2020.105126>.
- [24] X.Y. Cui, C. Tang, Q. Zhang, A review of electrocatalytic reduction of dinitrogen to ammonia under ambient conditions, *Adv. Energy Mater.* 8 (2018), 1800369, <https://doi.org/10.1002/aenm.201800369>.
- [25] C. Yang, B. Huang, S. Bai, Y. Feng, Q. Shao, X. Huang, A generalized surface chalcogenation strategy for boosting the electrochemical N₂ fixation of metal

- nanocrystals, *Adv. Mater.* 32 (2020), 2001267, <https://doi.org/10.1002/adma.202001267>.
- [26] L. Zhang, M. Cong, X. Ding, Y. Jin, F. Xu, Y. Wang, L. Chen, L. Zhang, A Janus Fe-SnO₂ catalyst that enables bifunctional electrochemical nitrogen fixation, *Angew. Chem. Int. Ed.* 59 (2020) 10888–10893, <https://doi.org/10.1002/anie.202003518>.
- [27] Y. Guo, Q. Yang, D. Wang, H. Li, Z. Huang, X. Li, Y. Zhao, B. Dong, C. Zhi, A rechargeable Al-N₂ battery for energy storage and highly efficient N₂ fixation, *Energy Environ. Sci.* 13 (2020) 2888–2895, <https://doi.org/10.1039/d0ee01241f>.
- [28] T.N. Ye, S.W. Park, Y. Lu, J. Li, M. Sasase, M. Kitano, H. Hosono, Contribution of nitrogen vacancies to ammonia synthesis over metal nitride catalysts, *J. Am. Chem. Soc.* 142 (2020) 14374–14383, <https://doi.org/10.1021/jacs.0c06624>.
- [29] R. Hao, W. Sun, Q. Liu, X. Liu, J. Chen, X. Lv, W. Li, Y.P. Liu, Z. Shen, Efficient electrochemical nitrogen fixation over isolated Pt sites, *Small* 16 (2020), 2000015, <https://doi.org/10.1002/smll.202000015>.
- [30] B. Chang, L.Q. Deng, S.Z. Wang, D. Shi, Z.Z. Ai, H.H. Jiang, Y.L. Shao, L. Zhang, J. X. Shen, Y.Z. Wu, X.P. Hao, A vanadium–nickel oxynitride layer for enhanced electrocatalytic nitrogen fixation in neutral media, *J. Mater. Chem. A* 8 (2020) 91–96, <https://doi.org/10.1039/c9ta11378a>.
- [31] J. Jia, T.L. Xiong, L.L. Zhao, F. Wang, H. Liu, R. Hu, J. Zhou, W.J. Zhou, S.W. Chen, Ultrathin N-Doped Mo₂C nanosheets with exposed active sites as efficient electrocatalyst for hydrogen evolution reactions, *ACS Nano* 11 (2017) 12509–12518, <https://doi.org/10.1021/acsnano.7b06607>.
- [32] Y.Y. Ma, T. Yang, H.Y. Zou, W.J. Zang, Z.K. Kou, L. Mao, Y.P. Feng, L. Shen, S. J. Pennycook, L.L. Duan, X. Li, J. Wang, Synergizing Mo single atoms and Mo₂C nanoparticles on CNTs synchronizes selectivity and activity of electrocatalytic N₂ reduction to ammonia, *Adv. Mater.* 32 (2020), e2002177, <https://doi.org/10.1002/adma.202002177>.
- [33] B.B. Fan, H.Z. Wang, H. Zhang, Y. Song, X.R. Zheng, C.J. Li, Y.Q. Tan, X.P. Han, Y. D. Deng, W.B. Hu, Phase transfer of Mo₂C induced by boron doping to boost nitrogen reduction reaction catalytic activity, *Adv. Funct. Mater.* 32 (2022), 2110783, <https://doi.org/10.1002/adfm.202110783>.
- [34] Y. Song, H.Z. Wang, Z.X. Song, X.R. Zheng, B.B. Fan, X.P. Han, Y.D. Deng, W.B. Hu, Ni-doped Mo₂C anchored on graphitized porous carbon for boosting electrocatalytic N₂ reduction, *ACS Appl. Mater. Interfaces* 14 (2022) 17273–17281, <https://doi.org/10.1021/acsami.2c00280>.
- [35] L.L. Zhao, H.F. Yuan, D.H. Sun, J. Jia, J.Y. Yu, X. Zhang, X. Liu, H. Liu, W.J. Zhou, Active facet regulation of highly aligned molybdenum carbide porous octahedrons via crystal engineering for hydrogen evolution reaction, *Nano Energy* 77 (2020), 105056, <https://doi.org/10.1016/j.nanoen.2020.105056>.
- [36] X. Ren, J. Zhao, Q. Wei, Y. Ma, H. Guo, Q. Liu, Y. Wang, G. Cui, A.M. Asiri, B. Li, B. Tang, X.P. Sun, High-performance N₂-to-NH₃ conversion electrocatalyzed by Mo₂C nanorod, *ACS Cent. Sci.* 5 (2019) 116–121, <https://doi.org/10.1021/acscentsci.8b00734>.
- [37] Y. Liu, X.R. Zhu, Q.H. Zhang, T. Tang, Y. Zhang, L. Gu, Y.F. Li, J.C. Bao, Z.H. Dai, J. S. Hu, Engineering Mo/Mo₂C/MoC hetero-interfaces for enhanced electrocatalytic nitrogen reduction, *J. Mater. Chem. A* 8 (2020) 8920–8926, <https://doi.org/10.1039/D0TA03290E>.
- [38] J.Y. Yu, B. Chang, W.Q. Yu, X. Li, D. Wang, Z. Xu, X. Zhang, H. Liu, W.J. Zhou, Chromium phosphide nanoparticles embedded in porous nitrogen-/phosphorus-doped carbon as efficient electrocatalysts for a nitrogen reduction reaction, *Carbon Energy* 4 (2022) 237–245, <https://doi.org/10.1002/cey2.160>.
- [39] H. Palneedi, J.H. Park, D. Maturya, M. Peddigari, G.T. Hwang, V. Annapureddy, J. W. Kim, J.J. Choi, B.D. Hahn, S. Priya, K.J. Lee, J. Ryu, Laser irradiation of metal oxide films and nanostructures: applications and advances, *Adv. Mater.* 30 (2018), 1705148, <https://doi.org/10.1002/adma.201705148>.
- [40] J. Berzins, S. Indrisiunas, K. van Erve, A. Nagarajan, S. Fasold, M. Steinert, G. Gerini, P. Gecys, T. Pertsch, S.M.B. Baumer, F. Setzpfandt, Direct and high-throughput fabrication of Mie-Resonant metasurfaces via single-pulse laser interference, *ACS Nano* 14 (2020) 6138–6149, <https://doi.org/10.1021/acsnano.0c01993>.
- [41] Z. Li, J.-Y. Fu, Y. Feng, C.-K. Dong, H. Liu, X.-W. Du, A silver catalyst activated by stacking faults for the hydrogen evolution reaction, *Nat. Catal.* 2 (2019) 1107–1114, <https://doi.org/10.1038/s41929-019-0365-9>.
- [42] B. Ravel, M. Newville, ATHENA, ARTEMIS, HEPHAESTUS: data analysis for X-ray absorption spectroscopy using IFEFFIT, *J. Synchrotron Radiat.* 12 (2005) 537–541, <https://doi.org/10.1107/S0909049505012719>.
- [43] S.I. Zabinsky, J.J. Rehr, A. Ankudinov, R.C. Albers, M.J. Eller, Multiple-scattering calculations of x-ray-absorption spectra, *Phys. Rev. B Condens. Matter* 52 (1995) 2995–3009, <https://doi.org/10.1103/physrevb.52.2995>.
- [44] L.F. Greenlee, J.N. Renner, S.L. Foster, The use of controls for consistent and accurate measurements of electrocatalytic ammonia synthesis from dinitrogen, *ACS Catal.* 8 (2018) 7820–7827, <https://doi.org/10.1021/acscatal.8b02120>.
- [45] Y. Zhao, R. Shi, X. Bian, C. Zhou, Y. Zhao, S. Zhang, F. Wu, G.I.N. Waterhouse, L. Z. Wu, C.H. Tung, T.R. Zhang, Ammonia detection methods in photocatalytic and electrocatalytic experiments: how to improve the reliability of NH₃ production rates? *Adv. Sci.* 6 (2019), 1802109, <https://doi.org/10.1002/adv.201802109>.
- [46] P. Saha, S. Amanullah, A. Dey, Electrocatalytic reduction of nitrogen to hydrazine using a trinuclear nickel complex, *J. Am. Chem. Soc.* 142 (2020) 17312–17317, <https://doi.org/10.1021/jacs.0c08785>.
- [47] G. Kresse, D. Joubert, From ultrasoft pseudopotentials to the projector augmented-wave method, *Phys. Rev. B* 59 (1999) 1758–1775, <https://doi.org/10.1103/PhysRevB.59.1758>.
- [48] J.P. Perdew, K. Burke, M. Ernzerhof, Generalized gradient approximation made simple, *Phys. Rev. Lett.* 77 (1996) 3865–3868, <https://doi.org/10.1103/PhysRevLett.77.3865>.
- [49] P.E. Blochl, Projector augmented-wave method, *Phys. Rev. B Condens. Matter* 50 (1994) 17953–17979, <https://doi.org/10.1103/physrevb.50.17953>.
- [50] H.J. Monkhorst, J.D. Pack, Special points for Brillouin-zone integrations, *Phys. Rev. B* 13 (1976) 5188–5192, <https://doi.org/10.1103/PhysRevB.13.5188>.
- [51] J. Harl, L. Schimka, G. Kresse, Assessing the quality of the random phase approximation for lattice constants and atomization energies of solids, *Phys. Rev. B* 81 (2010), 115126, <https://doi.org/10.1103/PhysRevB.81.115126>.
- [52] J. Wang, B. Huang, Y. Ji, M. Sun, T. Wu, R. Yin, X. Zhu, Y. Li, Q. Shao, X.Q. Huang, A general strategy to glassy M-Te (M = Ru, Rh, Ir) porous nanorods for efficient electrochemical N₂ fixation, *Adv. Mater.* 32 (2020), 1907112, <https://doi.org/10.1002/adma.201907112>.
- [53] Y. Zhao, F. Li, W. Li, Y. Li, C. Liu, Z. Zhao, Y. Shan, Y. Ji, L. Sun, Identification of M-NH₂-NH₂ intermediate and rate determining step for nitrogen reduction with bioinspired sulfur-bonded FeW catalyst, *Angew. Chem. Int. Ed.* 60 (2021) 20331–20341, <https://doi.org/10.1002/anie.202104918>.
- [54] L. Shi, Y. Yin, S. Wang, X. Xu, H. Wu, J. Zhang, S. Wang, H. Sun, Rigorous and reliable operations for electrocatalytic nitrogen reduction, *Appl. Catal. B Environ.* 278 (2020), 119325, <https://doi.org/10.1016/j.apcatb.2020.119325>.
- [55] B.H.R. Suryanto, H.-L. Du, D. Wang, J. Chen, A.N. Simonov, D.R. MacFarlane, Challenges and prospects in the catalysis of electroreduction of nitrogen to ammonia, *Nat. Catal.* 2 (2019) 290–296, <https://doi.org/10.1038/s41929-019-0252-4>.
- [56] S.Z. Andersen, V. Colic, S. Yang, J.A. Schwalbe, A.C. Nielander, J.M. McEnaney, K. Enemark-Rasmussen, J.G. Baker, A.R. Singh, B.A. Rohr, M.J. Statt, S.J. Blair, S. Mezzavilla, J. Kibsgaard, P.C.K. Vesborg, M. Cargnello, S.F. Bent, T.F. Jaramillo, I.E.L. Stephens, J.K. Nørskov, I. Chorkendorff, A rigorous electrochemical ammonia synthesis protocol with quantitative isotope measurements, *Nature* 570 (2019) 504–508, <https://doi.org/10.1038/s41586-019-1260-x>.
- [57] R.Y. Hodgetts, A.S. Kiryutin, P. Nichols, H.-L. Du, J.M. Bakker, D.R. MacFarlane, A. N. Simonov, Refining universal procedures for ammonium quantification via rapid ¹H NMR analysis for dinitrogen reduction studies, *ACS Energy Lett.* 5 (2020) 736–741, <https://doi.org/10.1021/acsenenergylett.9b02812>.
- [58] A.C. Nielander, J.M. McEnaney, J.A. Schwalbe, J.G. Baker, S.J. Blair, L. Wang, J. G. Pelton, S.Z. Andersen, K. Enemark-Rasmussen, V. Colic, S. Yang, S.F. Bent, M. Cargnello, J. Kibsgaard, P.C.K. Vesborg, I. Chorkendorff, T.F. Jaramillo, A versatile method for ammonia detection in a range of relevant electrolytes via direct nuclear magnetic resonance techniques, *ACS Catal.* 9 (2019) 5797–5802, <https://doi.org/10.1021/acscatal.9b00358>.
- [59] S. He, Z.J. Shao, Y. Shu, Z. Shi, X.M. Cao, Q. Gao, P. Hu, Y. Tang, Enhancing metal-support interactions by molybdenum carbide: An efficient strategy toward the chemoselective hydrogenation of alpha,beta-unsaturated aldehydes, *Chemistry* 22 (2016) 5698–5704, <https://doi.org/10.1002/chem.201600323>.
- [60] S.N. He, L. Xie, M.W. Che, H.C. Chan, L.C. Yang, Z.P. Shi, Y. Tang, Q.S. Gao, Chemoselective hydrogenation of α,β -unsaturated aldehydes on hydrogenated MoO_x nanorods supported iridium nanoparticles, *J. Mol. Catal. A Chem.* 425 (2016) 248–254, <https://doi.org/10.1016/j.molcata.2016.10.016>.
- [61] Y. Guo, Z. Yao, B.J.J. Timmer, X. Sheng, L. Fan, Y. Li, F. Zhang, L. Sun, Boosting nitrogen reduction reaction by bio-inspired FeMoS containing hybrid electrocatalyst over a wide pH range, *Nano Energy* 62 (2019) 282–288, <https://doi.org/10.1016/j.nanoen.2019.05.051>.
- [62] L. Zhang, X. Ji, X. Ren, Y. Ma, X. Shi, Z. Tian, A.M. Asiri, L. Chen, B. Tang, X.P. Sun, Electrochemical ammonia synthesis via nitrogen reduction reaction on a MoS₂ catalyst: theoretical and experimental studies, *Adv. Mater.* 30 (2018), 1800191, <https://doi.org/10.1002/adma.201800191>.
- [63] Y. Tian, B. Chang, G. Wang, L. Li, L. Gong, B. Wang, R. Yuan, W. Zhou, Magnetron sputtering tuned “ π back-donation” sites over metal oxides for enhanced electrocatalytic nitrogen reduction, *J. Mater. Chem. A* 10 (2022) 2800–2806, <https://doi.org/10.1039/d1ta10273g>.